TÉCNICO LISBOA

Porous Electrodepositions Influence on Conical Flames Stability in Unconfined Single-point Injection Burners

André Henriques Marques Neves

Thesis to obtain the Master of Science Degree in

Mechanical Engineering

Supervisors: Prof. Edgar Caetano Fernandes
Dr. Luísa Maria Leal da Silva Marques

Examination Committee

Chairperson: Prof. João Orlando Marques Gameiro Folgado
Supervisor: Prof. Edgar Caetano Fernandes
Member of the Committee: Prof. Gonçalo Nuno de Oliveira Duarte

November 2018

Dedicado à minha família.

Acknowledgments

Aqui pretendo prestar os meus mais sinceros agradecimentos e devido reconhecimento a todos os que me apoiaram nesta importante fase da minha vida que culmina com a realização deste trabalho.

Em primeiro lugar, quero agradecer ao Professor Edgar Fernandes e à Doutora Luísa Marques pelo acompanhamento prestado no decurso deste trabalho. Toda a disponibilidade apresentada para troca de ideias e esclarecimento de dúvidas não só enriqueceu o trabalho realizado como teve uma forte contribuição no meu desenvolvimento pessoal. Em seguida, expressar o meu agradecimento ao Tiago Oliveira e ao João Cunha por todas as sugestões fornecidas e apoio prestado, fundamentais para enfrentar as dificuldades encontradas.

A um nível mais pessoal, quero agradecer encarecidamente a toda a minha família, especialmente aos meus pais, Paulo Neves e Fátima Henriques, e ao meu avô Albino Henriques pelos sacrifícios a que se sujeitaram para que chegasse a este ponto. Não podia deixar de enaltecer os meus amigos de faculdade, que me acompanharam e apoiaram neste percurso académico: Alexandre Ferro, Miguel Viana, João Vital, Aldo Schaaf, Mariana Cunha, Raquel Miranda, Gil Santos, entre muitos outros. Por último, um especial agradecimento aos amigos sem os quais esta experiência não teria sido igual: Sebastião Perdigão, Vítor Martins, Manuel Gambôa, João Lourenço, André Monteiro, Manuel Teles, João Alves, João Uva, André André, Rita Rodrigues, Rafael Oliveira e Henrique Massano.

Resumo

No sentido de expandir esta análise para chapas multi-perfuradas, este trabalho avalia a influência de deposições específicas na parede interna do furo da chapa de ancoragem na estabilidade de um queimador aberto com uma só perfuração.

Utilizando o método *dynamic hydrogen bubble template* (DHBT), quatro electrodeposições porosas foram realizadas. As Amostras A e B (*coatings*) correspondem a coberturas finas do chanfro da chapa, enquanto as Amostras C e D (*fillings*) tratam-se de espumas grandes reconstrutoras do mesmo. A Amostra A apresentou maioritariamente cobalto (Co) na sua composição, com morfologia estilo favo de mel; as Amostras B, C e D exibiram essencialmente um derivado de zinco (Zn), morfologicamente composto por sub-unidades hexagonais. A Amostra D apresentou interconexão de poros.

Para espessuras características de electrodeposições industriais, a estabilidade de uma chapa chanfrada não é relevantemente afectada pela condutividade térmica do revestimento do chanfro (λ) ou pela sua variação durante a operação ($\frac{\partial \lambda}{\partial T}$).

Uma reconstrução porosa do chanfro numa chapa chanfrada, que restringe a passagem do escoamento de aproximação no fundo da chapa, pode afetar a dinâmica da chama a um nível tal que, para uma condição de combustão instável, o seu acoplamento prévio com a acústica do queimador é interrompido, estabilizando.

Uma reconstrução porosa do chanfro numa placa chanfrada, com dimensão de poro apropriada e alto nível de interconexão, mitiga o desenvolvimento de instabilidades termo-acústicas, aparentemente através de um aumento dos efeitos termoviscosos locais e do consequente aumento da dissipação acústica do queimador.

Palavras-chave: Estabilidade de chama, instabilidades termo-acústicas, electrodeposições porosas, chapa perfurada, dinâmica de chama, acústica do queimador

Abstract

With a future purpose to expand the analysis to multiperforated plate burners, the present work evaluates the flame stability influence of specific surface manipulations of the anchoring plate's perforation inner wall in an unconfined single-perforated plate burner.

Using the dynamic hydrogen bubble template (DHBT) method, four 3D porous electrodepositions were performed in upward chamfered plates. Samples A and B were considered coatings, thin layers covering the plate's chamfer, while Samples C and D were termed fillings, large foams reconstructing the plate's chamfer. Sample A was mainly composed by cobalt (Co), presenting a honeycomb-like structure, but Samples B, C and D were essentially composed by a zinc (Zn)-derived (simonkolleite), presenting a morphology embodied by hexagon-like sub-units. Sample D was the only one presenting pore interconnectivity.

For the thickness intervals characteristic of industrial applications of electrodepositions, flame stability in an upward chamfered plate isn't relevantly affected by the chamfer's coating thermal conductivity (λ) or its variation during operation ($\frac{\partial \lambda}{\partial T}$).

A porous reconstruction of an upward chamfered plate's chamfer, which restricts the incoming reactant flow crossing area at the plate's bottom, might affect the flame's dynamics to a point where, for a particular unstable operating condition, its former coupling with the (unaltered) burner's acoustics is disrupted.

A porous reconstruction of an upward chamfered plate's chamfer, with a high pore interconnectivity level and an appropriately tuned pore size, mitigates the flame's ability to develop self-sustained thermoacoustic instabilities, apparently by increasing the local thermoviscous effects and consequently enhancing the burner's acoustic damping.

Keywords: Flame stability, thermoacoustic instabilities, 3D porous electrodepositions, single-perforated plate, flame's dynamics, burner's acoustics

Contents

List of Tables

List of Figures

Nomenclature

Chemical species

C_3H_8	Propane.
C	Carbon.
Cl	Chloride.
$CoCl_2.6H_2O$	Cobalt chloride hexahydrate.
CO	Carbon monoxide.
Co	Cobalt.
H^+	Hydrogen free radical.
H_2	Hydrogen molecule.
H	Hydrogen atom.
NaCl	Sodium chloride.
NH_4Cl	Ammonium chloride.
NO_2	Nitrogen dioxide.
NO	Nitric oxide.
NO_X	Nitrogen oxide.
O	Oxygen.
$ZnCl_2$	Zinc chloride.
$Zn_5(OH)_6(Cl)_2.H_2O$	Zinc-derived (simonkolleite).
Zn	Zinc.

Greek symbols

λ	Thermal conductivity.
λ_{wave}	Wavelength.

μ Dynamic viscosity.

μ_{mix} Reactant mixture dynamic viscosity.

ϕ Equivalence ratio.

ϕ' Equivalence ratio fluctuations.

π Pi number.

ρ Density.

ρ' Density fluctuations.

ρ_{mix} Reactant mixture density.

θ Polar angle coordinate.

Roman symbols

a Stoichiometric coefficient of oxygen for complete propane combustion in air.

A_{exp} Substrate area exposed to electrodeposition.

A_f Instantaneous flame area.

A'_f Instantaneous flame area fluctuations.

D Resonant cavity internal diameter.

d Anchoring plate perforation bottom diameter.

ϵ_Q Flow rate relative error.

I Electric current.

i Current density.

L Resonant cavity length.

l Anchoring plate thickness.

M Molar mass.

$\dot{m_{dry\,air}}$ Dry air mass flow rate.

$\dot{m_{C_3H_8}}$ Propane mass flow rate.

p' Pressure fluctuations.

Q' Flame heat release fluctuations.

$Q_{dry\,air}$ Dry air measured flow rate.

$Q_{C_3H_8}$ Propane measured flow rate.

Q_m Measured flow rate.

Q_{max} Maximum flow rate capacity.

Q_{total} Global measured flow rate.

Re Reynolds number.

S'_L Laminar flame speed fluctuations.

t Anchoring plate perforation top diameter.

t_{exp} Substrate exposure time to electrodeposition.

u' Velocity fluctuations.

U_{mix} Reactant mixture average velocity.

U_ϕ Equivalence ratio total uncertainty.

U_Q Flow rate total uncertainty.

$U_{Q_{dry\,air}}$ Dry air measured flow rate total uncertainty.

$U_{Q_{C_3H_8}}$ Propane measured flow rate total uncertainty.

$U_{Q_{total}}$ Global measured flow rate total uncertainty.

U_{Re} Reynolds number total uncertainty.

$x_{O_2}^{air}$ Average molar fraction of oxygen present in the atmosphere at sea level.

Subscripts

st Stoichiometric conditions.

Glossary

DHBT	Dynamic Hydrogen Bubble Template.
EDS	Energy Dispersive Spectrometer.
FSD	Flame Stability Diagram.
FTF	Flame Transfer Function.
MPP	Multiperforated Plate.
PTFE	Polytetrafluoroethylene.
PW	Pressure Wave.
SEM	Scanning Electron Microscopy.
SLPM	Standard Liter Per Minute.
SPL	Sound Pressure Level.
SS	Stainless steel.
STP	Standard Temperature and Pressure.
XRD	X-Ray Diffraction.

Chapter 1

Introduction

1.1 Motivation

Since 1950, unprecedented social and technological developments have lead to an increase in the world's average lifespan and enabled better living conditions for the majority of humankind. This has led to an exponential increase in the world's population: it has more than doubled since 1970 and is expected to achieve 10 billion people by 2055 [1].

This growth has propelled global energy demand, whose evolution in the last 27 years is presented in Figure 1.1[1] by source type. Although environmental considerations will force us to alter the observed source distribution, the reality is that in 2016 more than 90% of the world's energy production came from fossil fuels, biofuels and waste.

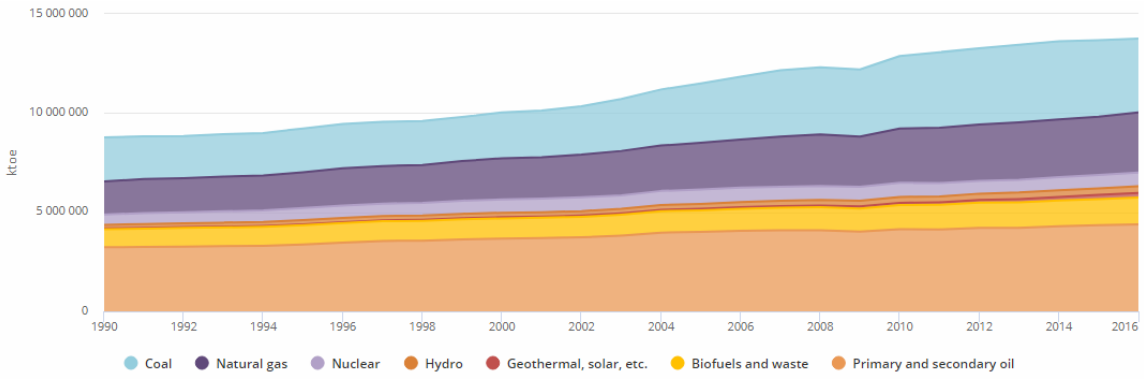

Figure 1.1: Global energy production by source type from 1990 to 2016. (Source: International Energy Agency)

However, like in most primary energy sources, the form on which this natural energy presents itself must be changed to enable its final consumption. Regarding the fuels presented in Figure 1.1, their chemical energy must be converted into thermal energy (mainly) by the process of combustion, as schematically represented in Figure 1.2. Defined as the science of exothermic chemical reactions in flows with heat and mass transfer by Liñán and Williams [2], combustion's strong exothermic behaviour is precisely what guarantees this reaction's critical role in global energy production, but also invites its

[1] 1 ktoe $= 4.1868 \times 10^4$ GJ (Source: International Energy Agency)

employment in several other areas, such as the transport industry (e.g. internal combustion engines), the space industry (e.g. rocket propulsion systems) or the heating industry (e.g. domestic boilers).

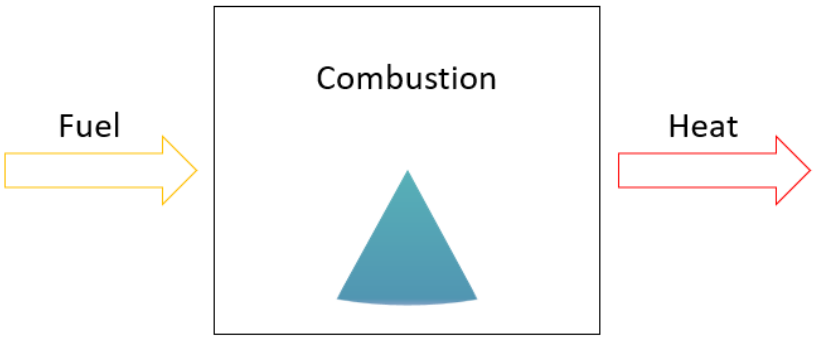

Figure 1.2: Conversion of the chemical energy intrinsic to fuels into thermal energy through combustion.

Nonetheless, the combustion of the aforementioned hydrocarbon fuels presents grave environmental and health implications due to the pollutant and toxic character of some of its products. The ones which today present a major public concern are: nitrogen oxides (NO_X) - mainly nitric oxide (NO) and nitrogen dioxide (NO_2) - toxic gases that contribute to the formation of smog, acid rain and gorund-level ozone; and carbon monoxide (CO), toxic gas which may be responsible for most of fatal air poisonings in several industrial countries up to 2002 [3].

To enable a reduction of these pollutants emissions, the combustion industry's policies have changed to operate in low temperature and low fuel conditions, increasingly working at lean regimes. Although these conditions effectively mitigate NO_X emissions, if unchecked they may still lead to problematic CO levels [4] and, more than that, they worsen the flame's acoustic behaviour, facilitating the occurrence of combustion instabilities [5].

In regard to the thermotechnology industry specifically, these environmental concerns have changed the way open flame burners are designed. To obtain a required heat output, instead of using a flame anchoring surface with a single large perforation where a single hot flame anchors, a surface with several small perforations where several smaller and colder flames anchor is used. Among other designs, this has given rise to multiperforated burners, as the ones depicted in Figure 1.3, whose application varies from industrial dryers to domestic boilers, presented in Figure 1.4.

However, complementing the above-mentioned depiction, the low flame temperature conditions in which these multiperforated burners are operated and the strong flame-flame interactions inherent to their design make them increasingly more prone to the occurrence of thermoacoustic instabilities than a single-perforation configuration [5, 6].

With the exception of some devices specifically designed to operate in oscillatory conditions (e.g. dump combustors or pulse combustors), not encompassed in the analysed industry, these instabilities are highly undesirable [7]. They can lead to large amplitude oscillations in the system: decreasing its performance level, by inducing high whistling noises and augmenting heat fluxes to the burner's boundaries [8], and reducing its life cycle while increasing safety hazards, by unpredictably decreasing its parts life [9] and possibly leading to structural damage.

Figure 1.3: Multiperforated burner designs. Left: Sabaf Flat burner. (Source: Sabaf) Right: Bekaert Multipat premix burner. (Source: Bekaert)

Figure 1.4: Applications for multiperforated burners. Left: NSI Equipments Rotary drum dryer. (Source: NSI Equipments) Right: Fondital MINORCA KC (High Efficiency). (Source: Fondital)

Historically, these combustion-driven acoustic oscillations were corrected by trial-and-error design of the burner, but due to a growing need to operate in very large modulation ranges this method has become non-viable. Hence, an accurate acoustic modelling of the system has become a critical part of its design phase, in an attempt to minimize such oscillations for all required operating conditions [5].

1.2 Thermoacoustic instabilities

Although this phenomenon has been known for around 150 years, a concise and fulfilling definition of it is often neglected in the researched literature. Despite this, thermoacoustic instabilities can be interpreted as unsteady high-speed variations of the flame's heat release based on a flame-burner acoustic coupling, governed by the flame's dynamics and the burner's acoustic characteristics. Examples of a flame in a stable and unstable condition are provided in Figure 1.5.

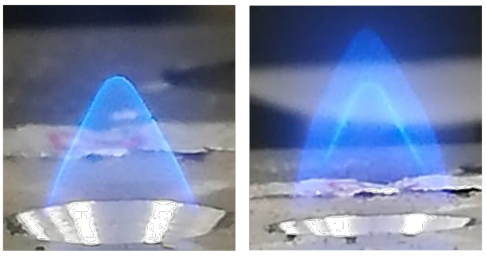

Figure 1.5: Thermoacoustic instabilities in a conical premixed flame. On the left, a stabilized flame; on the right, a thermoacoustically unstable flame.

As described by Candel [10], combustion instabilities are a consequence of the interaction between at least two physical mechanisms: a driving process responsible to induce perturbations in the reactant flow and a feedback process which couples the perturbations' effects to the initial driving mechanism. Although several processes like structural vibrations or convective modes may establish the required feedback, acoustic wave propagation is the most common source of flame-burner coupling and thus will be the effect considered in the present work.

A schematic description of the cyclic interaction underlying pressure-coupled instabilities is provided in Figure 1.6. The phenomenon is initiated by the action of a certain driving mechanism which directly induces velocity fluctuations (u') in the flow inside the burner's cavity or indirectly through the generation of local pressure oscillations (p'). These downstream velocity fluctuations are then convected by the flow until they reach the upstream flame front, which separates the fresh reactants region from the different density burned products region, deforming it. This interaction will alter the flame's instantaneous surface area (A_f) and variate its local temperature and equivalence ratio (ϕ), causing density and laminar flame speed fluctuations (ρ' and S'_L, respectively). These effects will induce heat release oscillations (Q') in the flame, leading to the emission of pressure waves (PWs) that propagate (almost) isotropically across the surrounding medium [11]. When these interact with the downstream burner cavity, the later acts as resonant filter, producing an amplified interior PW at a frequency given by the overlap between the flame-generated PW's frequencies and the burner's acoustic response to an external excitation [12]. Finally, these cavity-generated pressure fluctuations affect once more the reactant's flow velocity profile, closing the feedback cycle.

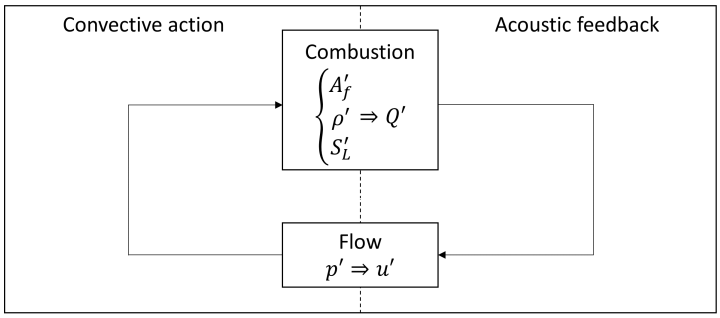

Figure 1.6: Schematic depiction of the flame-burner acoustic coupling.

Although the depicted interaction occurs with some regularity, it does not always induce a state of oscillatory combustion. As described by Schuller *et al.* [6] and Noiray *et al.* [8], for self-sustained thermoacoustic instabilities to naturally arise in open flame configurations, 3 conditions must be satisfied:

- An overlap between the frequency bandwidth of the burner's response to an excitation and the frequencies of the flame-generated PW must occur. This will enable the burner's generation of an interior PW and allow the possible establishment of the acoustic-flame coupling mechanism.
- The acoustic energy produced by the unsteady combustion must be fed into the burner (i.e. the flame-generated PW must be in phase with the flow when arriving at the burner's outlet). This will create a constructive feedback response, ensuring the onset of self-induced thermoacoustic instabilities in the system.

- The acoustic energy generated by the flame, the active element, should exceed the acoustic energy dissipated inside the burner, the passive element. This will guarantee the system's self-induced thermoacoustic instabilities are also self-sustained.

Nonetheless, the harmful effects associated to these instabilities have strongly encouraged the exploration of practical control methods to mitigate or extinguish them in commercial applications. From the existing reviews, some authors can be recognized such as McManus *et al.* [13] and Richards *et al.* [14] for their work in confined burner configurations or Noiray *et al.* [8] for his studies in unconfined ones. Generally, acoustic control methods are divided into two groups: active control solutions and passive control solutions.

As presented by [13], active control solutions intend to condition the system's stability based on a time-varying adjustment, relying on control systems whose operation depends on a dynamic hardware component (actuator). Usual dynamic components applied include acoustic driver units, used to excite a combustor in an attempt to disrupt its flame-flow phase alignment, and servo valves, meant to control its incoming flow rates and produce a time-variation in its operating condition.

Passive control solutions on the other hand change flame stability trough time-fixed modifications, without resorting to any actuators [13]. Existing approaches typically attempt to avoid a coincidence between the burner's frequency bandwidth and the flame's unstable frequency ranges, disabling the flame-burner acoustic coupling. This can be achieved by changes to the burner's acoustics or variations to the flame's convective time delay (i.e. time taken for the velocity perturbations to travel from the burner's outlet to the flame's tips [12]). While the former can be obtained by appropriate hardware and design modifications, the latter may rely on using multiple time lags, combining fuel injectors with different dynamic response (in the case of enclosed-flame configurations) or adding diffusion pilot flames (despite their significant NO_X emissions) [14].

In conclusion, despite the significant potential of active control methods, regarding their capability to readjust combustion dynamics and accommodate externalities like changing ambient conditions or fuel composition [14], they encompass several practical problems. In this context, the combustion industry, especially the heating industry, has focused primarily on passive control solutions whose simplicity facilitates its commercial applicability [8].

1.3 Surface manipulation techniques

Surface engineering procedures have lately been growing in importance, being relevant in a variety of areas such as the energy storage industry (e.g. supercapacitors) or the chemical engineering industry (e.g. heterogeneous catalytic reactors). There are several methods which allow to deposit different layers over a structure's surface (substrate), depending on such surface characteristics and on the substances to deposit [15, 16]. These techniques allow to control the substrate's functional properties and improve them according to its application, whether it is increasing its resistance to corrosion or decreasing its thermal conductivity.

According to Meille [15], most traditional depositions are based on a liquid phase and can be divided into: suspensions - based on the dispersion of a finished material to be deposited; sol-gel depositions - based on a solution of a chemical precursor of the material to deposit; and powder plasma sprays - based on a spray of the suspended powder to be deposited. Although these methods are flexible enough to enable the creation of a wide variety of deposition conditions, they involve a complex chemical preparation which severely increases the sample production time. For instance, the sol-gel deposition technique requires the production of a chemical precursor solution which, depending on the substrate size and the desired coating characteristics (particularly its thickness), may take several weeks [15]. It may be also necessary to improve the adhesion between the coating layer and the substrate, resorting to binding solutions whose preparation time may be equally long. This makes the deposition process very time-consuming; which is particularly enviable in a scenario where the testing of a large variety of deposition conditions is critical.

In such scenario, a non-traditional deposition method is required, steering the search towards electrochemical deposition: process where a metal, metal oxide, polymer or composite coating is produced on a desired surface through the action of an electric current. This method is a well-established, one-step, low cost and flexible technique whose scale-up and mass-production are viable, being present across various industrial lines [16].

The principle behind this technique is a simple reduction-oxidation reaction occurring near the surface to be coated, as described in Figure 1.7. Using an electrolytic cell, a working electrode, represented by the substrate, and a counter electrode are immersed in a previously prepared aqueous solution rich in the salt of the metal to be deposited, acting as an electrolyte. Using a power supply, an electric current is applied between the substrate, acting as the cathode, and the counter electrode, acting as the anode, forcing the positively charged metal ions present in the solution to migrate towards the negatively charged substrate. There, the former ions are reduced and form a metallic deposit which covers the active surface [15]. This procedure is normally conducted in the solvent window of the electrolyte, where the reduction of the solvated metal ions takes place without interference from solvent decomposition [17].

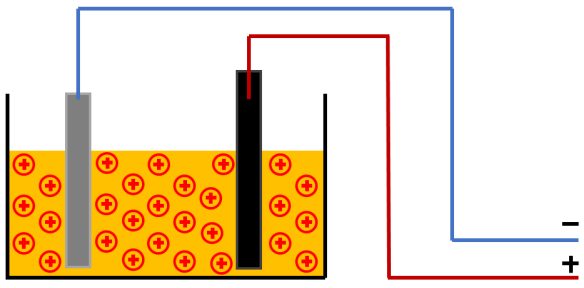

Figure 1.7: Schematic description of the working principle behind electrodeposition.

To conduct this procedure, several parameters must be controlled, being the most important ones: the electrolyte's composition, the applied current density (i[2]) and the substrate's exposure time (t_{exp}).

[2] $i = \frac{I}{A_{exp}}$, where I is the electric current generated between electrodes and A_{exp} is the substrate's surface area exposed to

The combination of these parameters determines the produced coating's characteristics, namely its composition, its morphology and its thickness; allowing to obtain a variety of structures, from homogeneous dense layers to highly porous deposits [16].

For a certain aqueous electrolyte in contact with a metallic substrate, Plowman *et al.* [17] states that an appropriate tuning of i and t_{exp} can be used to create porous metallic foams with high surface areas, employing the dynamic hydrogen bubble template (DHBT) method. In this method, when current is applied, metal nuclei formation at the substrate's active sites is accompanied by hydrogen (H) evolution (H^+ reduction to H_2), leading to local production and release of hydrogen bubbles. These bubbles provide shielding to the active sites and consequently alter the electromagnetic field generated between electrodes, concentrating the induced current lines around the H_2 bubbles and on the already formed metal nuclei. This disrupts the metal growth mechanism and generates macropores within the developing structure, increasing its specific surface area. When the applied current ceases, the hydrogen evolution process terminates and the developed metallic foam remains attached to the substrate. This way, H_2 bubbles act as a negative dynamic template around which metal grows, forming a porous foam structure. This method's great advantage relies on allowing a reasonably easy control of the deposition's pore size and morphology without the use of an additional template, through a delicate balance between the H_2 bubbles nucleation and the metal deposits growth [17]. The DHBT method is schematically illustrated in Figure 1.8.

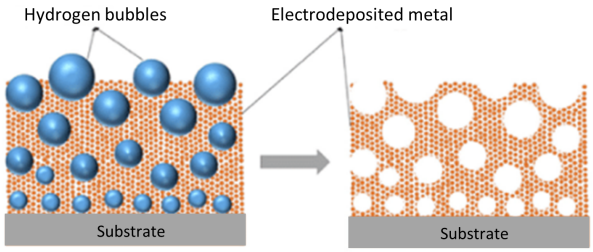

Figure 1.8: Schematic description of the DHBT method.

As described, the characteristics of electrochemical depositions are a direct result of their fabrication method and not of additional post treatments, which provides them a high degree of reproducibility that facilitates the technique's industrial implementation [16].

1.4 State of the art

Attempting to fulfill the aforementioned need to accurately model the acoustic behaviour of modern open flame heating systems, an extensive research has been performed on several types of configurations. From that, a few studies can be denoted.

Durox *et al.* [7] exposed the importance of flame-wall interactions as a driving mechanism for self-induced thermoacoustic instabilities. The work analysed the arise of such instabilities on a premixed cool central core laminar flame anchored on a cylindrical burner and impinging on a flat plate facing its

metal deposition.

outlet. An instability model was devised describing the resonant feedback created between the flame's interaction with the downstream cold plate and the upstream burner's acoustics.

Such study relied on the previous developments made by Schuller *et al.* [11] which successfully described the relations between the unsteady combustion process and the consequently emitted PW. The article investigated the flame noise generation process in an acoustically excited premixed laminar flame impinging on a cooled plate. A model was presented characterizing the link between the radiated PWs, the flame's chemiluminescence and the flame's instantaneous surface area A_f.

Following the work of Durox *et al.* [7], Schuller *et al.* [6] established the role of mutual flame interactions as a driving mechanism for self-sustained thermoacoustic instabilities. The study evaluated the unstable behaviour of a premixed laminar "M" flame anchored on an annular burner. An instability model based on energy considerations was constructed for this case, decomposing the problem into an analysis of the burner's acoustics and a study of the flame's response to forced flow oscillations. This yielded important criteria for the onset and maintenance of the flame's unstable behaviour, which are in agreement with the Rayleigh criterion [18].

Later, Noiray *et al.* [19] attempted a greater approximation to burner geometries used in industrial process applications; studying the development of self-sustained thermoacoustic instabilities on premixed conical laminar flames anchored on a multiperforated plate (MPP) burner. An instability model was engineered by defining a dispersion relation for the reactive system, combining: the flames response to an external perturbation, the sound radiated by the unstable flames and the perforated plate acoustic impedance.

Continuing this investigation, Noiray *et al.* [8] presented passive control solutions to suppress combustion-driven instabilities by controlling the plate's thickness and the perforations' diameter. Utilizing the same setup as [19], an instability model based on energy considerations was devised using an oscillatory circuit analogy (similar to the one used by Schuller *et al.* [6]). This led to instability criteria which are in line with [6] but provided greater physical meaning, allowing the deduction of passive control solutions to mitigate the undesired instabilities. The first consisted on increasing the plate's thickness to decrease the acoustic power provided to the burner and increase the system's acoustic damping, narrowing its unstable frequency ranges. The second relied on varying the perforations' diameter at a constant porosity to change the flames' dynamics and shift its transfer function (FTF) frequency-wise, in an attempt to avoid an overlap between the unstable flame emitted PWs' frequencies and the burner's eigenfrequencies, breaking the acoustic-flame coupling cycle.

More recently, Ferreira [20] introduced the importance of the plate's perforation ratio in the development of self-sustained thermoacoustic instabilities on an MPP burner. Using the same setup as Noiray *et al.* [19], the work analysed the stability of premixed conical laminar flames. An instability model based on energy considerations was devised, breaking down the problem into an analysis of the burner's acoustics and a study of the flames' dynamics. The burner's acoustic impedance was computed using Tijdeman [21] description of wave propagation in cylindrical tubes, applying the Low Frequency method, and Maa [22] empirical inclusion of the perforation ratio; while the flames' acoustic impedance was deduced using the relations between the radiated pressure waves and the flame's surface area A_f [8] and

an analytical approximation for the FTF of conical flames measured by Fernandes and Leandro [12].

Although the presented models have contributed to a greater understanding of the complex phenomenon that are thermoacoustic instabilities, the strong dependence between the occurrence of such phenomenon and the nature of the flame's dynamics and the burner's acoustics has made it difficult to derive a reliable generalist approach that enables to predict and prevent such behaviour [8]. Most models present simplifications and are case-specific to particular types of burner design or operating conditions, being extremely difficult and time-consuming to adapt to the wide variety of cases encountered in the heating industry reality.

Nonetheless, the literature still presents several ways flame stability can be improved in an industrial scenario, as depicted in Section 1.2. The present review inserts itself in this area of study.

1.5 Objective

To facilitate its industrial implementation, the objective of the present work is to provide a basis for the creation of a simple and flexible passive method to minimize the development of self-sustained thermoacoustic instabilities in modern open flame MPP burners.

To maximize the obtained solution's application limits, the mitigation of the flames' unstable behaviour should be achieved by enabling an increase of the system's acoustic damping and not by avoiding an overlap between the burner's frequency bandwidth and the flame's unstable frequency ranges. Although some acoustic dissipation occurs inside the burner's resonant cavity and at the perforations' outlet, the burner's acoustic resistance is essentially determined by the thermoviscous effects in the perforations' inner wall boundary layer [8].

Hence, the present study focuses on manipulating such wall surface conditions by applying different depositions and analysing the influence of those depositions on flame stability.

1.6 Thesis outline

This document is organized into four different chapters. Chapter 1 starts by presenting the motivation behind the work conducted, followed by an exposure of the main theoretical concepts regarding thermoacoustic instabilities and a literature review on the subject. It finishes with the establishment of the long-term and short-term objectives of this work. In Chapter 2 is provided an extensive description on the experimental apparatus used and on the applied experimental techniques. Chapter 3 presents the obtained experimental results and its physical interpretation. It is divided into two sections: Section 3.1 provides an extensive characterization of the considered deposition samples and Section 3.2 concerns the flame stability analysis performed under different experimental conditions. Finally, Chapter 4 summarizes the work's major conclusions and provides some recommendations regarding the further exploration of this subject.

Chapter 2

Experimental setup

2.1 Setup description and operation

The flame's stability was examined in an unconfined single-point injection configuration, where a premixed air-propane conical laminar flame is anchored on a single-perforation plate. The burner configuration is presented in Figure 2.1 and was inspired by the one used by Noiray *et al.* in the studies presented in Section 1.4.

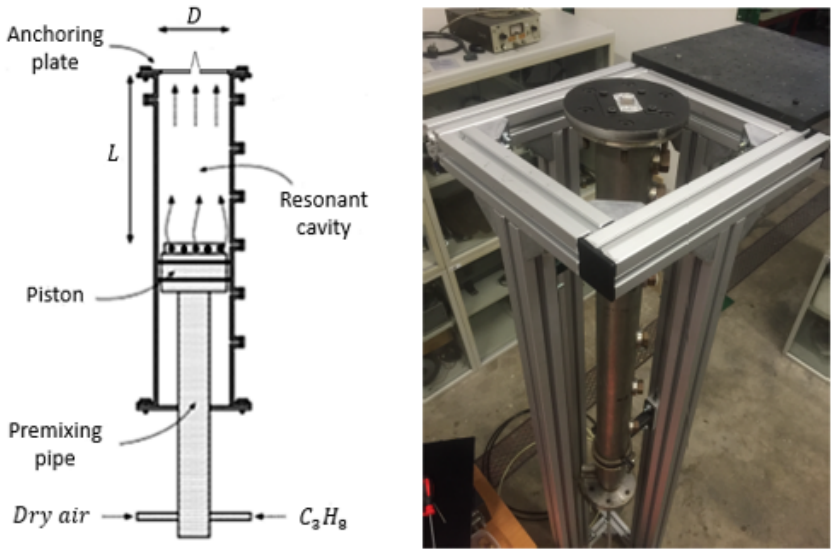

Figure 2.1: Single-perforated plate burner. Left: Schematic depiction of the burner apparatus used. Right: Burner structure.

The system is essentially comprised by a premixing pipe, a resonant cavity and a single-perforation plate. The reactant mixture is injected into a "V" shape connection at the lower part of the premixing pipe, where it flows up to the resonant cavity and is fed to it through twelve apertures around the piston's head, which presents a 42 mm diameter. The resonant duct presents a 43,5 mm internal diameter (D) and a variable length (L) defined by the piston's head position, allowing to control the burner's acoustic behaviour. It is enclosed at its bottom by the piston's flat head, establishing a quasi-perfect acoustical

reflection boundary, and at its top by the single-perforation plate, where the conical flame anchors. This forms an unconfined reaction zone which reproduces to some extent the conditions found in some modern heating devices [8]. The annular gap between the piston and the resonant duct is sealed with an O-ring made of polytetrafluoroethylene (PTFE). The geometrical characteristics of the system's resonant cavity are exposed in Table 2.1.

Table 2.1: Geometrical dimensions of the burner's resonant cavity.

Resonant duct	mm
Length L	10$< L <$700
Internal diameter D	43.5

In line with the presented objective to minimize flame instabilities in MPP burners, an anchoring plate with multiple perforations would be the natural choice for the tested configuration. However, a single-perforation plate was considered more appropriate for the present work's focus: to evaluate the performed depositions effects on the flame's behaviour; since it facilitated the flame's visualization and it decoupled the influence of flame-flame interaction from the results obtained.

Several assumptions were performed in this investigation, from which the most relevant ones can be presented:

- The air and the propane are in STP conditions, at a temperature of 25º C and a pressure of 101.32 kPa;
- The air-propane mixture is perfectly mixed when it enters the resonant cavity;
- The reactant flow is laminar and presents top-hat velocity distribution at the anchoring plate's outlet;
- The driving mechanism responsible for the development of acoustic instabilities is mutual flame interaction between opposing reactive fronts, where flame-noise generation is due to sudden quenching at the flame's tips and burning of the consequently formed fresh reactant pockets;
- Flame-generated PWs propagate isotropically;
- The cavity's diameter to length ratio ($\frac{D}{L}$) is sufficiently small compared to the flame oscillation frequencies, that only longitudinal acoustic modes (planar waves) may install in it;

The system's stability is conditioned by the flame's dynamics and the burner's acoustics. The former is determined by the reactant flow's Reynolds number (Re) and equivalence ratio (ϕ), while the latter is controlled by the resonant cavity length L, whose variation translates in a shift of the burner's frequency bandwidth when exposed to an external excitation, emulating the acoustics of a variety of commercial burners.

In the conducted stability analysis, the fuel used was propane (C_3H_8) and the oxidizer was atmospheric dry air, filtered using a water filter. Tests were performed using an experimental setup schematically depicted in Figure 2.2.

The gases flow rates were controlled using two precision gas flow meters (Alicat Scientific, MC series) with maximum capacities of 5 and 1 standard liter per minute (SLPM). The controllers were

assigned to each gas according to the maximum mass flow rate required for the experimental tests, using the 5-SLPM controller for the air and 1-SLPM controller for the propane. Both controllers were operated using the Flow Vision^{TM} software with an user interface developed in LabVIEW.

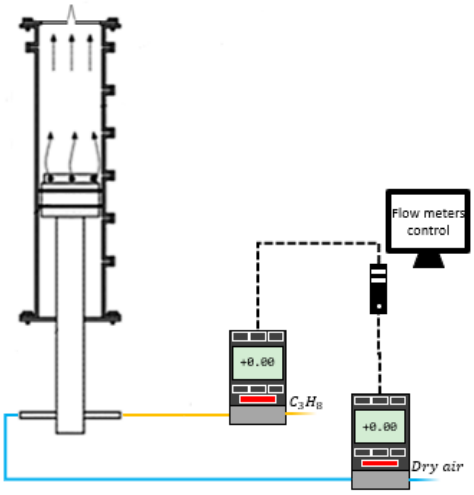

Figure 2.2: Schematic representation of the experimental setup used for flame stability analysis.

For a defined resonant duct length L, tests were conducted at constant equivalence ratios sweeps: for each ϕ, the mixture's Re was lowered from blowoff conditions to (or near) flashback, starting at rich values and then decreasing ϕ to leaner regimes. For each point of interest, an average of at least three measurements was performed and flame instability was recognized trough flame visualization and hearing. The maximum thermal power yielded in the operated conditions was 3.7 kW.

The flow's control parameters Re and ϕ were defined by Equations 2.1 and 2.2:

$$Re = \frac{\rho_{mix} U_{mix} d}{\mu_{mix}} \tag{2.1}$$

$$\phi = \frac{\frac{\dot{m_{C_3H_8}}}{\dot{m_{dry\,air}}}}{\left(\frac{\dot{m_{C_3H_8}}}{\dot{m_{dry\,air}}}\right)_{st}} \tag{2.2}$$

where ρ_{mix} and μ_{mix} are the mixture's density and dynamic viscosity respectively, d is the plate's perforation bottom diameter, U_{mix} is the mixture's flow velocity while crossing d's corresponding area, $\dot{m_{C_3H_8}}$ and $\dot{m_{dry\,air}}$ are respectively the mass flow rate of the fuel and the oxidizer and the subscript st refers to such quantities in stoichiometric conditions.

For each operating condition, the mixture's density ρ_{mix} was calculated from the ideal gas law [23], while its velocity U_{mix} was obtained through the continuity equation [23]. The mixture's dynamic viscosity μ_{mix} was computed as a weighted average of each gas's dynamic viscosity. Table 2.2 presents the gases properties at STP conditions.

The calibrated gas flow meters used in the present experiments have an uncertainty associated to their output which, by means of error propagation, affects the flow control parameters used: Re and ϕ.

The total uncertainty associated to each controller's flow rate (U_Q) is defined by the joint contribution

Table 2.2: Gases properties at STP conditions.

Property	**Air**	**Propane C_3H_8**
M (kg/kmol)	28.96	44.09
μ ($Pa^{-6}s$)	18.492	8.146
ρ (kg/m^3)	1.184	1.832

of its reading uncertainty (0.8%) and scale uncertainty (0.2%), as determined by Equation 2.3:

$$U_Q = \pm(0.008Q_m + 0.002Q_{max}) \tag{2.3}$$

where Q_m is the controller's measured flow rate for a given working condition and Q_{max} is the controller's maximum flow rate capacity. An attempt to diminish the uncertainty associated to the experimental tests relied on using flow meters with the lowest possible maximum flow rate capacity. Using U_Q, the highest tested flow rate condition was taken to compute the maximum uncertainty associated to each controller's measured flow rate and its respective error (ϵ_Q). Results are presented in Table 2.3.

Table 2.3: Uncertainty and relative error associated to each flow meter for highest tested flow rate condition.

Gas	Q_m (SLPM)	Q_{max} (SLPM)	U_Q	ϵ_Q (%)
C_3H_8	0.243	1	$\pm$0.003944	1.623
$dry\,air$	3.672	5	$\pm$0.039376	1.072
Total	3.915	6	$\pm$0.043320	1.107

Analysing ϵ_Q's effect on the Re values obtained, the definition proposed in Equation 2.1 can be altered to explicit its dependence on the total working flow rate (Q_{total}), since $Q_{total} = U_{mix}(\pi/4)d^2$, obtaining Equation 2.4:

$$Re = \frac{4\rho_{mix}}{\pi\mu_{mix}d}Q_{total} \tag{2.4}$$

Neglecting possible density and geometric uncertainties, this formulation can be extended to express U_{Re} instead of Re in function of $U_{Q_{total}}$ instead of Q_{total}. Using this relation and the data presented in Table 2.3, the uncertainty and error associated to the measured Re can be quantified. These values are presented in Table 2.4 for the highest flow rate condition.

Table 2.4: Uncertainty and relative error associated to Re for highest tested flow rate condition.

$U_{Q_{total}}$ (SLPM)	Re	U_{Re}	ϵ_{Re} (%)
$\pm$0.043320	950	$\pm$10.504999	1.11

Analysing ϵ_Q's impact on the ϕ values attained, the definition proposed in Equation 2.2 can be altered to explicit its dependence on the propane and dry air flow rate ($Q_{C_3H_8}$ and $Q_{dry\,air}$, respectively), obtaining Equation 2.5:

$$\phi = \frac{aQ_{C_3H_8}}{x_{O_2}^{air}Q_{dry\,air}} \tag{2.5}$$

where a is the stoichiometric coefficient of oxygen for complete propane combustion and $x_{O_2}^{air}$ is the

average molar fraction of oxygen present in the atmosphere at sea level.

For complete propane-air combustion, $a = 5$ and $x_{O_2}^{air}$ was assumed equal to 0.2095 [24]. Neglecting the reactants density uncertainties, the equivalence ratio uncertainty (U_ϕ) can be ascertained with Equation 2.6:

$$U_\phi = \pm \frac{5}{0.2095 Q_{dry\,air}} \sqrt{U_{Q_{C_3H_8}}^2 + \left(\frac{Q_{C_3H_8} U_{Q_{dry\,air}}}{Q_{dry\,air}}\right)^2} \tag{2.6}$$

Using this relation and the data presented in Table 2.3, the uncertainty and error associated to the measured ϕ can be computed. These values are shown in Table 2.5 for the highest flow rate condition.

Table 2.5: Uncertainty and relative error associated to ϕ for the highest tested flow rate condition.

$U_{Q_{C_3H_8}}$ (SLPM)	$U_{Qdry\,air}$ (SLPM)	ϕ	U_ϕ (%)	ϵ_ϕ (%)
± 0.003944	± 0.039376	1.6	± 0.030724	1.92

2.2 Anchoring plates preparation

For the present stability tests, four single-perforation plates were used, presented in Figure 2.3. They can be divided into two types according to their perforation design, as straight edge perforation plates (SE plate) or upward chamfered plates (Benchmark plate and plates I and II). Plates I and II[1] were the ones used to evaluate the performed depositions influence on the flame's stability.

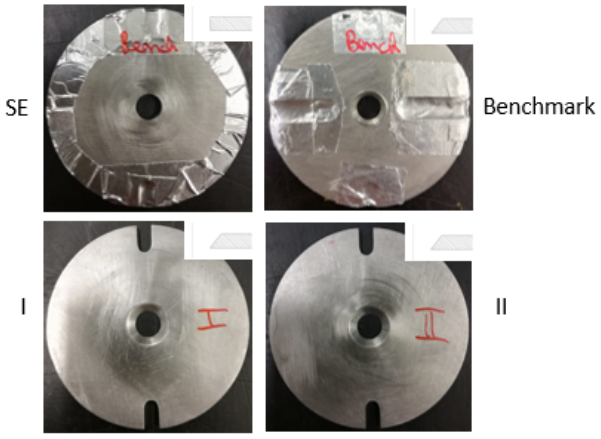

Figure 2.3: Single-perforation flame-anchoring plates. SE: straight edge plate; Benchmark: Benchmark plate; I: Plate I; II: Plate II. All plates present a chamfered perforation, except for the SE plate which presents a straight perforation.

All plates are made of stainless steel (SS) with a 2 mm thickness (l) and a perforation with a 6 mm bottom diameter. However, while the SE plate presents a straight perforation, with equal bottom and top diameter, the other plates present a (roughly) 45° upward chamfer, with a 6 mm bottom diameter d and a 10 mm top diameter (t). The full geometrical parameters of each plate may be checked in Table 2.6.

The straight perforations were made using laser cutting techniques, due to its smoother surface finish when compared to other drilling methods, and the chamfers, for the upward chamfered plates, were

[1] Two identical plates, plates I and II, were used in this investigation in an attempt to maximize the number of deposition conditions tested.

Table 2.6: Geometrical dimensions of the flame-anchoring plates (in mm).

Single-perforation plate	**SE**	**Benchmark**	**I**	**II**
Thickness l	2			
Perforation bottom diameter d	6			
Perforation top diameter t	6	10		

manually performed using a chamfer milling cutter. Measurements performed by Ferreira [20] showed that perforations made by laser cutting in SS plates exhibited slightly different diameters depending on the plate's side (less than 6%), such that the side with a halo around the hole was smaller. Hence, all experiments were conducted with the non-halo side facing the upstream fresh flow and the chamfers were created by widening the halo side; guaranteeing the reactant flow's crossing area at the plate's bottom is equal for all plates.

In alignment with the present work's ultimate goal to devise a stability solution applicable to an industrial scenario, an anchoring plate with a straight edge perforation would be the instinctive choice for the tested layout, given the design's wide commercial application. However, at this initial stage of investigation, the analysis of a large variety of deposition conditions was considered paramount, compelling the use of a perforation design which facilitated such depositions adhesion to its inner wall surface. Hence, the analysis of the depositions' influence on the flame's stability was performed using anchoring plates with an upward chamfered perforation, due to the increased support such perforation design provides.

2.2.1 Electrochemical deposition procedure

To perform the intended depositions in the inner chamfer surfaces of plates I and II, the technique of electrochemical deposition was elected due to the reasons exposed in Chapter 1.3.

Using plates I and II, a total of four deposition samples[2] were tested in this work, displayed in Figure 2.4. They can be divided into two groups depending on their architecture: as coatings (Samples A and B) – thin layers covering the plate's chamfer - or fillings (Samples C and D) – large deposits on the plate's chamfer aimed at reconstructing and "straighten" it, making its top diameter identical to the bottom one ($d = 6$ mm).

To perform such depositions, two precursor electrolyte solutions were prepared: one to deposit a zinc (Zn)-derived – containing 0.5 M $ZnCl_2$ (Sigma-Aldrich) and 2 M NH_4Cl (Roth) – and another to deposit cobalt (Co) – containing 0.1 M $CoCl_2.6H_2O$ (Roth), 1.5 M NH_4Cl (Roth) and 0.5 M NaCl (Sigma-Aldrich). Both solutions were prepared from analytical grade chemicals and distilled water. Previous to the electrodeposition, the plate to be deposited was cleaned with acetone in ultrasound and dried with a jet of cold air.

All electrodepositions were conducted employing the DHBT method at room temperature in an electrolytic cell, using a Kikusui Electronics power source (Model PAB 32-3). A graphite plate was used as a counter electrode, while the plate to be deposited was used as a working electrode, presenting an active surface area A_{exp} of 0.71 cm^2 (equal to its chamfer area). The experimental setup used to perform this

[2]Although additional deposition conditions were performed and tested throughout the investigation, only the electrodeposition samples which presented more meaningful results are presented and discussed in this review.

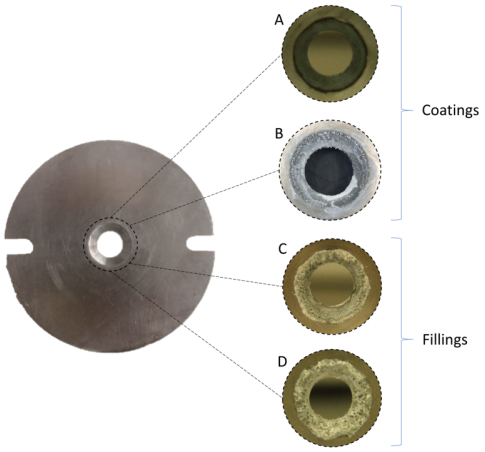

Figure 2.4: Synthesized electrodeposition samples. A: Sample A; B: Sample B; C: Sample C; D: Sample D. While Samples A and B correspond to chamfer coatings, Samples C and D correspond to chamfer fillings.

technique is presented in Figure 2.5.

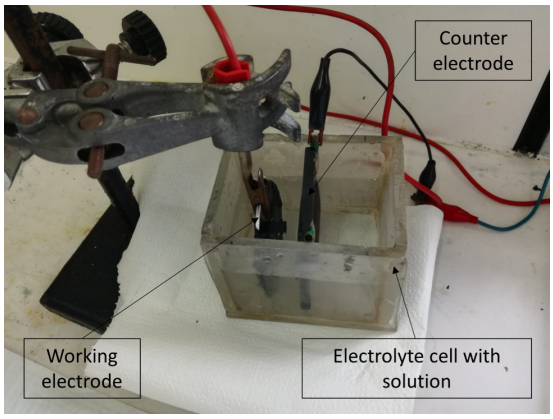

Figure 2.5: Experimental setup used for the electrochemical depositions.

Depending on the deposition sample, the procedure was carried out on a galvanostatic mode (constant current) or on a pulsed mode (pulsed current), for a defined exposure time. Each sample's electrodeposition parameters (electrolyte composition, i and t_{exp}) are summarized in Table 2.7. After this procedure, the deposited plate was rinsed in distilled water and left to dry for a day.

Table 2.7: Electrodeposition parameters used to synthesize each sample. Samples A, B and D were performed with constant current, while Sample C was obtained with pulsed current (30 s intervals).

Electrodeposition sample	**Electrolyte composition**	**Current density i (A/cm^2)**	**Exposure time t_{exp} (s)**
Sample A	0.1 M $CoCl_2.6H_2O$ + 1.5 M NH_4Cl + 0.5 M NaCl	0.37	180
Sample B	0.5 M $ZnCl_2$ + 2 M NH_4Cl	0.23	90
Sample C	0.5 M $ZnCl_2$ + 2 M NH_4Cl	3.45	420 (30s pulses)
Sample D	0.5 M $ZnCl_2$ + 2 M NH_4Cl	2.69	240

Given the high level growth of metallic deposits required to obtain the synthesized fillings (Samples C and D), during these samples' electrodeposition procedures, a cylindrical pin was placed inside the corresponding chamfered plate's perforation to provide interior support for the growing metal deposit and delimit its inner wall geometry and dimensions. The pin's presence would ensure the growing foam would present a fairly uniform inner diameter, equal to the plate's bottom diameter d, reconstructing the

chamfered perforation and ”straightening it”. To achieve this, the cylindrical pin was manufactured with a 5 mm length and a 5.5 mm diameter, so that when covered with electrical tape would practically present a diameter equal to d. The pin's placement inside the chamfered plate's perforation and its dimensions are schematically represented in Figure 2.6.

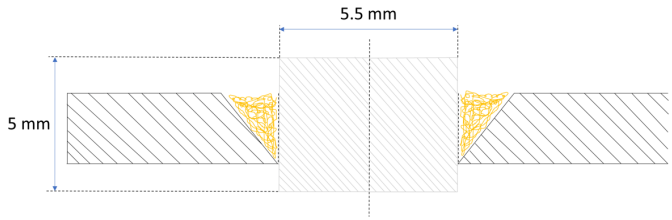

Figure 2.6: Cylindrical pin placement and dimensions during the synthesized fillings electrodepositions procedure.

2.3 Physico-chemical characterization of the deposition samples

The crystal structures of the synthesized deposition samples were investigated using X-ray diffraction[3] (XRD). Diffractograms were recorded at room temperature by a Bruker AXS-D8 Advance powder diffractometer with a Bragg-Brentano geometry [Cu Kα radiation source ($\lambda_{wave} = 0.150619\,$nm)] and the diffraction patterns were collected over a 2θ range of incidence angles from $10°$ to $90°$, with a $0.02°$ step size. The morphological characterization of these samples was performed using Scanning Electron Microscopy[4] (SEM, Hitachi S2400) and the elemental chemical analyses were performed by its corresponding Energy Dispersive Spectrometer (EDS). Figure 2.7 displays the equipment used to perform such characterization.

Figure 2.7: Equipments used for the physico-chemical characterization of the synthesized samples. Left: Bruker AXS-D8 Advance powder diffractometer. Right: Scanning Electron Microscope Hitachi S2400.

[3]X-ray diffraction is the elastic scattering of X-ray photons upon contact with the atoms of a prepared powdered sample. The intensity of the diffracted radiation in respect to the incidence angle can help characterize the atoms present in the sample [25].

[4]Scanning Electron Microscopy is used to study surface morphology and composition. A narrow electron beam is focused upon the surface and by tracking the direction of the scattered electrons in respect to the primary incidence direction, the surface topography is obtained [25].

Chapter 3

Results and Discussion

The obtained experimental results and their interpretation are hereby presented. Both quantitative and qualitative analysis are performed from the collected data.

In Section 3.1, an extensive characterization of the synthesized deposition samples is performed to enlighten the composition, morphological and architectural differences between them. In Section 3.2, flame stability maps measured under different experimental conditions are presented and discussed. Sub-section 3.2.1 exhibits a stability characterization of all the anchoring plates used in this work, in the absence of electrodepositions. Section 3.2.2 follows by presenting a set of deposition case-studies, intended to evaluate such depositions influence on the flame's stability and possibly identify its structural characteristics which may suppress the flame's unstable behaviour. This section finishes with a stability comparison between the best performing case uncovered in this work and the most industrially present perforation design.

3.1 Deposition samples characterization

From the four deposition samples tested in this investigation, two different compositions emerged: one in Sample A and another in Samples B, C and D.

Figure 3.1 shows the X-ray diffractogram of Sample A, presenting the intensity of its diffracted X-ray beams as a function of the incidence angle 2θ. According to Qin *et al.* [26], the diffraction peaks at the incidence angles of 44.4° and 76.2°, signalled by plus signals, can be respectively indexed to the (111) and (220) crystal planes of face-centered cubic Co, while the ones at 41.8° and 47.3°, also signalled by plus signals, can be respectively associated to the (100) and (101) crystal planes of hexagonal close-packed Co. This indicates the presence of Co arrays in the performed deposition. The relative sharpness of such diffraction peaks reflects the high crystallinity of the deposited Co. Moreover, the EDS analysis of this sample revealed the presence of Co (75.2 norm. at. %[1]), oxygen (O) (15 norm. at. %) and carbon (C) (9.8 norm. at. %), confirming the presented XRD results.

[1] The normalized atomic percentage (norm. at. %) represents the percentage of the total amount of atoms of a given substance out of the total number of atoms of every substance present in the studied sample.

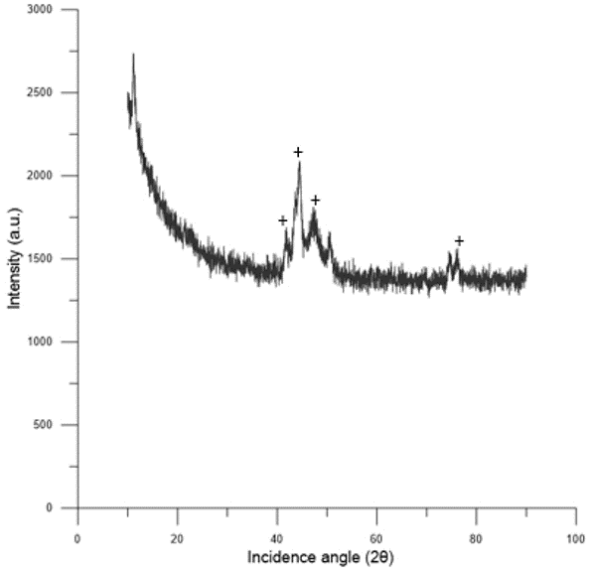

Figure 3.1: XRD pattern of Sample A.

Figure 3.2 presents the X-ray diffractogram of Samples B, C and D. The sharp intensity peaks indexed by an asterisk, particularly at the incidence angles of 11.3°, 28.3°, 32.9°, 36.2° and 58.3°, are characteristic of the cristal planes of hexagonal close-packed $Zn_5(OH)_6(Cl)_2.H_2O$ (simonkolleite) (RRUFF ID: R130117), indicating the presence of simonkolleite arrays with high crystalline purity in the performed depositions [27]. Furthermore, the EDS analysis of these samples revealed the presence of Zn (48.4 norm. at. %), O (39.7 norm. at. %) and chloride (Cl) (11.9 norm. at. %), supporting the shown XRD results.

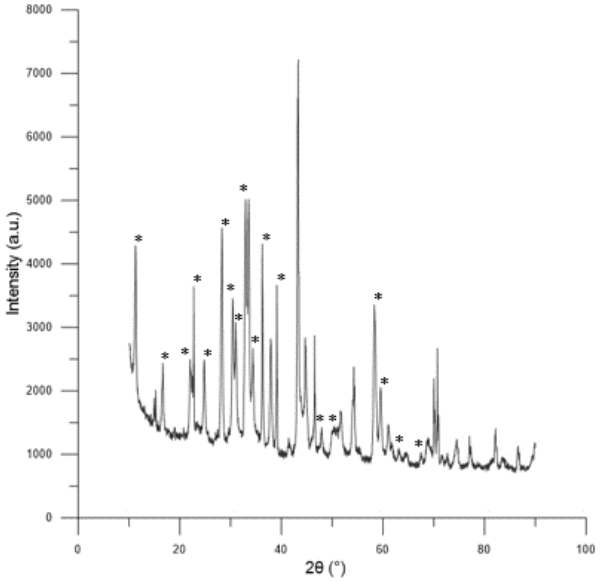

Figure 3.2: XRD pattern of Samples B, C and D.

The synthesized samples morphology can be visualized in Figure 3.3, where a 3D porous structure, typical of foams constructed by DHBT, is common to all cases. Nonetheless, there are still clear morphological differences between samples consequent of the electrodeposition parameters used for each:

while Sample A presents a honeycomb-like structure with relative homogeneity, as depicted by Plowman *et al.* [17], Samples B, C and D present a morphology composed by hexagon-like sub-units, typical of simonkolleite, as described by Marques *et al.* [27]. Also, while Sample D presents an interconnected network of pore walls, the other Zn-derived samples do not.

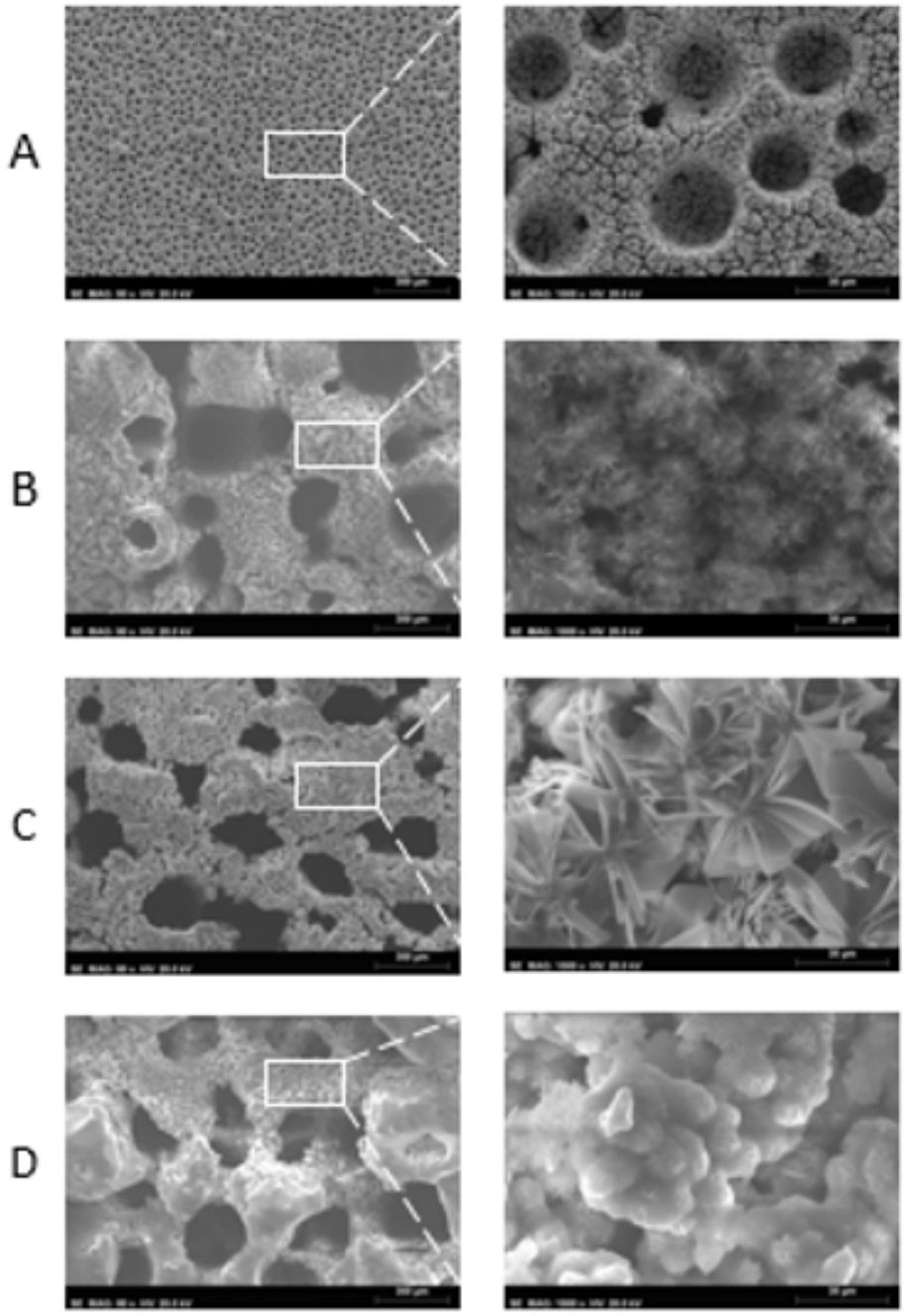

Figure 3.3: SEM micrographs showing top-down views of the synthesized samples. The images on the left correspond to a 80X amplification of the corresponding sample, while the images on the right correspond to a 1000X amplification of the area delimited in white.

Given its particular architecture, the synthesized fillings (Samples C and D) ability to reconstruct the corresponding plate's chamfer, using the interior support pin in the process, and "straighten" it, making the perforation's top diameter equal to its bottom, was evaluated. Using the Image J software, the

samples' top diameter was calculated from Figure 2.4 and compared to the plate's bottom diameter d. Results are presented in Table 3.1. As it shows, although both samples were not able to fully "straighten" the plate's chamfer perforation, Sample D performed a more complete chamfer reconstruction than Sample C.

Table 3.1: Geometrical dimensions of synthesized fillings (Samples C and D).

Filling	Perforation bottom diameter d (mm)	Reconstructed perforation top diameter (mm)	Reconstruction proximity (%)
Sample C	6	7.85	69.17
Sample D	6	6.67	88.83

3.2 Flame stability analysis

With a long-term view to mitigate self-sustained thermoacoustic instabilities in modern open flame MPP burners, flame stability diagrams (FSDs) under several experimental conditions (L, anchoring plate, deposition sample) were obtained for the unconfined single-point injection configuration described. These maps are here presented and a thorough physical interpretation of their results is performed.

3.2.1 Burner plates characterization

SE plate vs Benchmark plate

Considering the choice of using anchoring plates with an upward chamfered perforation to analyse the presented depositions influence on flame stability, instead of the more industrially present straight edge perforation design, it was important to first evaluate this perforation's geometry influence on the system's stability.

To do so, FSDs were measured for the burner using a straight edge perforation plate, SE plate, and an upward chamfered plate, Benchmark plate, for three different resonant cavity lengths, $L \in \{10.5, 20, 35\}$ (cm). Both plates' results were then compared with one another for every resonant cavity size in Figure 3.4.

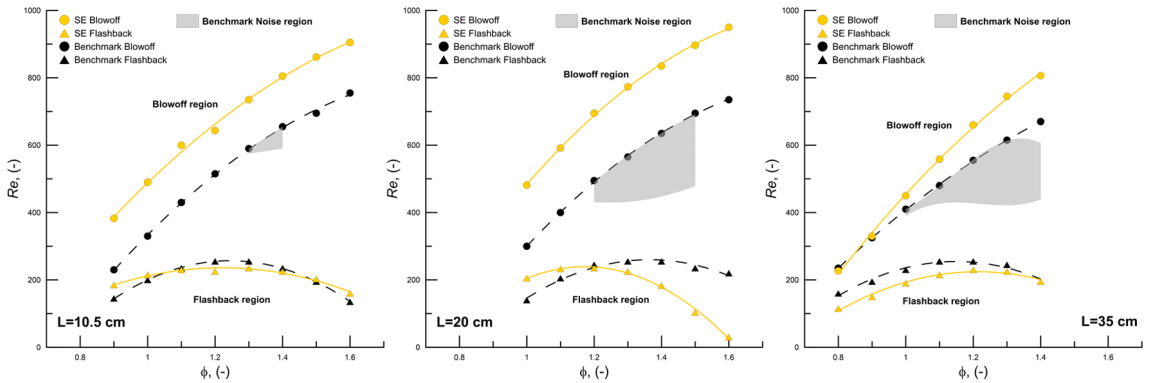

Figure 3.4: Overlap of the flame stability maps of the SE plate and the Benchmark plate for several resonant duct lengths. The map on the left was obtained for $L = 10.5$ cm, the map on the center was obtained for $L = 20$ cm and the map on the right was obtained for $L = 35$ cm. The SE plate is associated to yellow symbols while the Benchmark plate is associated to black symbols. The shaded area corresponds to Benchmark plate's self-sustained unstable combustion region.

For the considered equivalence ratios, the SE plate presents a higher flame stability than the Benchmark plate and while the former one does not induce self-sustained thermoacoustic instabilities, the latter one does. Besides this, although the SE plate's stability region is independent of the resonant duct length, the Benchmark plate's blowoff limit exhibits a slight variation with it, which becomes more noticeable for leaner ϕ. Finally, the Benchmark plate's instability region size varies with the burner's resonant cavity length.

Considering both plates present an identical perforation bottom diameter d and a small thickness l, the fresh reactant flow velocity profile at the plate's outlet is assumed equal in both cases; hence, the system with the highest laminar flame speed S_L should be the most stable one. According to Santos [28], for rich conditions ($\phi > 1$), the entrainment of the surrounding atmospheric air at the flame's base results in a dilution of the burning mixture, which approximates its equivalence ratio to stoichiometric conditions ($\phi \sim 1$). This will increase the flame's local burning temperature and consequently the local S_L. For lean conditions ($\phi < 1$), the opposite occurs and the mixture's dilution due to exterior air entrainment at the flame's base will move its equivalence ratio away from stoichiometric conditions, decreasing the S_L in that area.

For the entire operating conditions analysed, the Benchmark plate's flame is always inside its chamfer. There, due to the positive pressure induced by the upstream premixture flow, it is considered to be much less exposed to dilution from the surrounding air than the SE plate's flame. Thus, considering the results obtained by [28], while rich flames should be more stable in the SE plate, lean flames should be more stable in the Benchmark plate.

The results represented in Figure 3.4, somewhat translate this, particularly those for $L = 35$ cm where both rich and lean regimes were considered ($\phi \in [\,0.8, 1.4\,]$). In the latter, a crossing between the plates' blowoff lines occurs near $\phi = 0.85$, such that the SE plate is more stable for $\phi > 0.85$ and the Benchmark plate is more stable for $\phi < 0.85$.

Benchmark plate = function(L)

Considering the Benchmark plate's instability region variation with L depicted in Figure 3.4, a deeper characterization of its stability behaviour was required. Thus, its FSDs were acquired for a wider range of cavity sizes ($L \in [\,5, 40\,]$ (cm)) and compared with each other in Figure 3.5.

Although the flame's stability limits are fairly identical for all resonant duct lengths, there is a clear non-linear dependence between the size and location of the upward chamfered plate's acoustically unstable region and L. For the tested cavity sizes, such noise area is largest for $L \in \{20, 30, 35\}$ (cm) and smallest for $L \in \{5, 40\}$ (cm), qualitatively presenting, trough hearing, its highest sound pressure level (SPL) at $L = 35$ cm.

This non-linear behaviour is in agreement with the findings presented by [19] that, for a defined flame (constant Re and ϕ), conditions associated to acoustic instabilities alternate with ones characterized by stable combustion for a growing resonant cavity.

To properly evaluate the performed depositions influence on flame stability, the worst-case scenario was selected, studying such influence at the resonant cavity condition for which the Benchmark plate instability region was considerably large and its associated SPL was the highest, $L = 35$ cm.

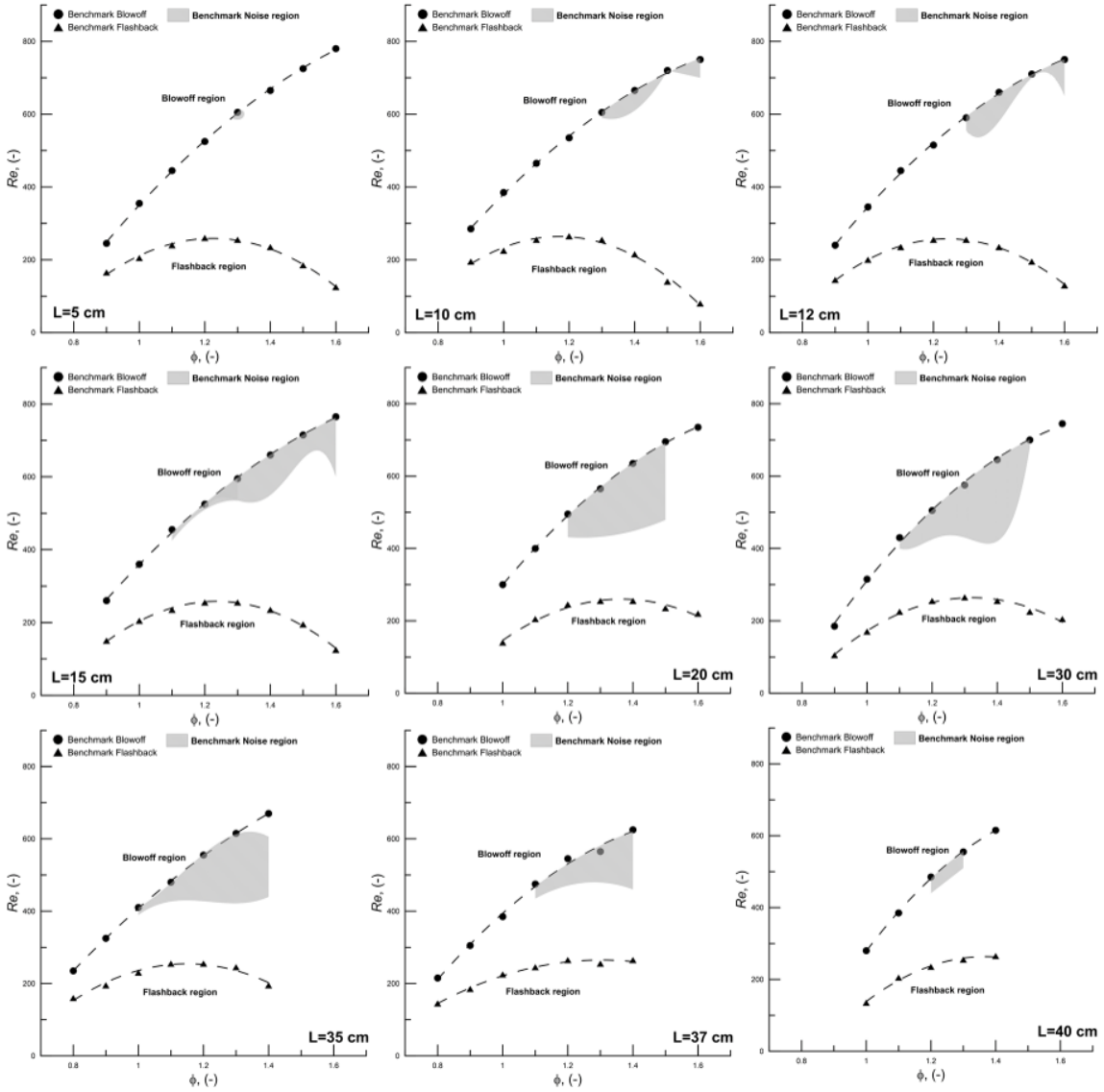

Figure 3.5: Flame stability maps of the Benchmark plate for a wide range of resonant duct lengths, $L \in \{5, 10, 12, 15, 20, 30, 35, 37, 40\}$ (cm). The shaded area corresponds to Benchmark plate's self-sustained unstable combustion region.

Plate I vs plate II

Having understood the influence of a chamfer perforation design and identified the resonant duct length at which combustion instabilities are more severe in the tested burner apparatus, a characterization of the upward chamfered plates effectively used to evaluate the performed depositions influence on flame stability (plates I and II) was imperative.

To do so, its FSDs were obtained for the defined resonant duct length ($L = 35$ cm) and compared with each other in Figure 3.6.

Albeit the plates were manufactured with the same techniques to present identical geometries and dimensions, they show different stability behaviours, with some variations around the position of their flammability limits and their respective noise regions. Nonetheless, such limits and noise regions maintain the same shape across both plates, presenting only an offset between them and thus suggesting that those differences are linear.

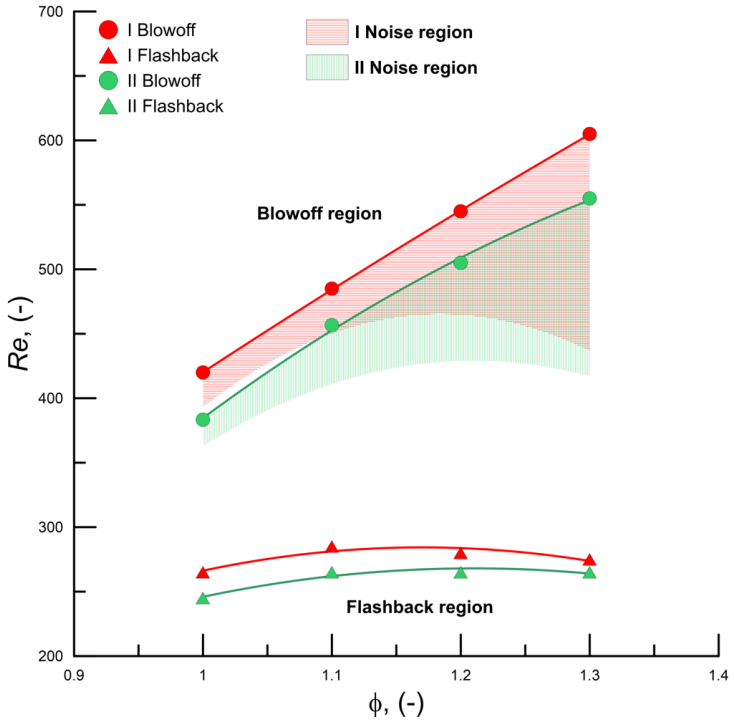

Figure 3.6: Overlap between plates I and II stability maps for $L = 35$ cm. Plate I is associated to red symbols while plate II is associated to green symbols. The red and green shaded areas correspond to plates' I and II self-sustained unstable combustion regions, respectively.

Such offset may be due to the fact that the plates chamfers were manually performed, which possibly has led to slightly different chamfer geometries that may have changed the flame-plate heat balance for each anchoring plate.

To prevent these differences from introducing errors in the present work's conclusions, plates I and II were treated as individually unique, such that the performed depositions influence on flame stability can only be evaluated by comparing the deposited plate's behaviour with the same plate's behaviour in the absence of electrodepositions.

3.2.2 Depositions case-studies

Addressing the present work's short-term objective to evaluate the characterized chamfer depositions influence on flame stability, a set of deposition case-studies is here presented. The performed analyses establish variations regarding: the thermal behaviour of the deposited material, the architecture of its macrostructure and the morphology of its microstructure.

Co coating vs Zn-derived coating

The first case-study intended to analyse the impact of the anchoring plate's chamfer thermal conductivity (λ) and its variation during operation ($\frac{\partial \lambda}{\partial T}$) in the flame's stability. To achieve this, plates' II and I chamfers were coated with Samples A and B, respectively. As described in Section 3.1, Sample A was essentially composed by Co, a material whose thermal conductivity is 100 W/(m*K) at STP conditions [29] but which decreases with temperature ($\frac{\partial \lambda}{\partial T} < 0$), acting as an insulating coating for the chamfer's surface. Sample B on the other hand was mainly composed by a Zn-derived (simonkolleite), a material

whose thermal conductivity is 116 W/(m*K) at STP conditions [29] but which increases with temperature ($\frac{\partial \lambda}{\partial T} > 0$), acting as a conductive coating for the chamfer's surface. To minimize the coatings' effect on the incoming flow's velocity profile at the plate's outlet, both samples' electrodeposition parameters were tuned to minimize their thickness and ensure a porous morphology.

Following this, the deposited plates' FSDs were acquired for the defined resonant duct length and compared to their respective behaviour in the absence of electrodepositions. Results are presented in Figure 3.7.

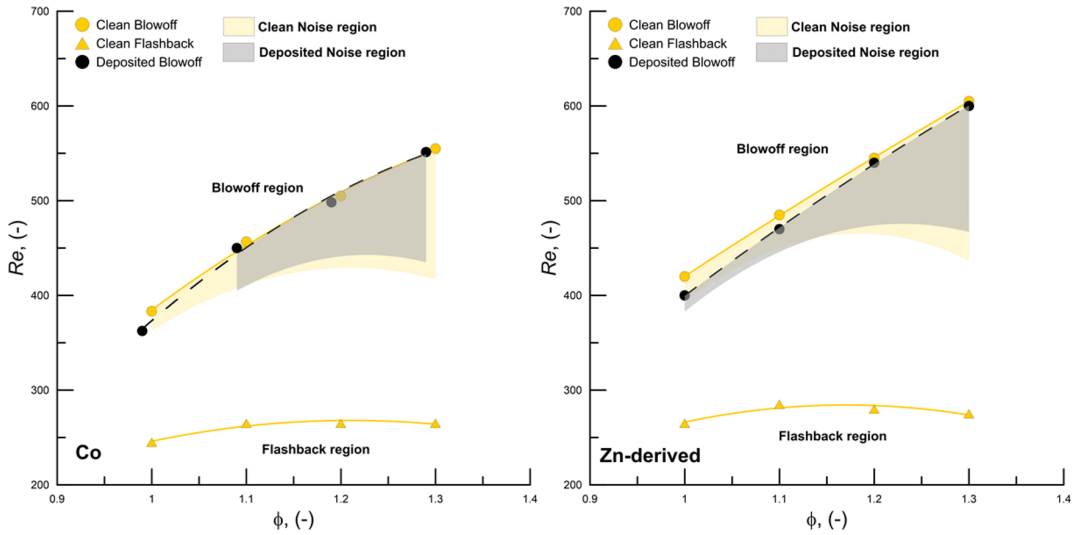

Figure 3.7: Overlap of plates' II and I stability maps in coated and non-coated conditions for $L = 35$ cm. The map on the left analyses the Co coating of plate II while the map on the right studies the Zn-derived coating of plate I. The non-deposited plate is associated to yellow symbols while the deposited plate is associated to black symbols. The yellow and grey shaded areas correspond to the non-deposited and deposited plates' self-sustained unstable combustion regions, respectively.

For both chamfer-coated plates, flame stability does not appear to be relevantly affected by the deposition's presence, presenting a blowoff limit identical to the one in non-deposited conditions and an instability region whose size and location is also reasonably similar to the one in clean conditions.

This may suggest that the plate's chamfer thermal conductivity λ does not significantly alter the flame-plate heat balance, hinting that the chamfer surface does not have a relevant role in flame stabilization. Nonetheless, considering the results presented in Figure 3.6 and theory on the stabilization mechanism of premixed flames, it is considered more likely that both coatings present such a small thickness that their impact on the chamfer's global conductive behaviour is negligible, making it perform identically regardless of the coatings presence.

As described by Kuczmarski and Johnston [30], the phenomenon of acoustic dissipation by means of a solid structure consists on the conversion of said acoustic energy into two main forms of energy: thermal energy, due to the viscous effects experienced inside the flowing medium and between it and the structure's surface, and strain energy, due to the deformation of the solid structure when interacting with the travelling pressure wave. A structure's capability to dissipate acoustic energy is therefore determined by its ability to foster these two energy conversions. A porous structure is particularly indicated for this, since it would allow the penetration of the exterior PW inside its matrix where it would be trapped in

a succession of reflections, transferring its energy to the structure in the form of frictional losses and deformations. The morphological characteristics which determine this structure's degree of efficacy are: its pore interconnectivity, the higher the more uniformly the exterior PW is dispersed through the matrix; and its pore size, if too coarse the PW will cross the structure with minimal interaction while if too fine it will not penetrate the surface enough to undergo a substantial level of interactions.

The depositions considered in the following case-studies were based on this insight, corresponding to large porous foams deposited on the plate's chamfer aimed at increasing the system's acoustic damping. Although this was not completely achieved, as exposed on Section 3.1, these foams intended to reconstruct the plates' chamfered-perforations, making its top diameter identical to the bottom one.

Filling with pin vs Filling without pin

The second case-study proposed to investigate the influence of the plate's chamfer filling architecture in the flame's stability. To do so, Sample C was deposited on both plates II and I, but while in the former one the aforementioned pin was placed inside its perforation during the electrodeposition procedure, to delimit the growing foam inner wall geometry and dimensions, in the latter it was not, allowing the deposition to evolve unrestrained during such time.

After this, the chamfer-reconstructed plates' FSDs were measured for the defined resonant duct length and compared to their respective "clean" performance. Results are presented in Figure 3.8.

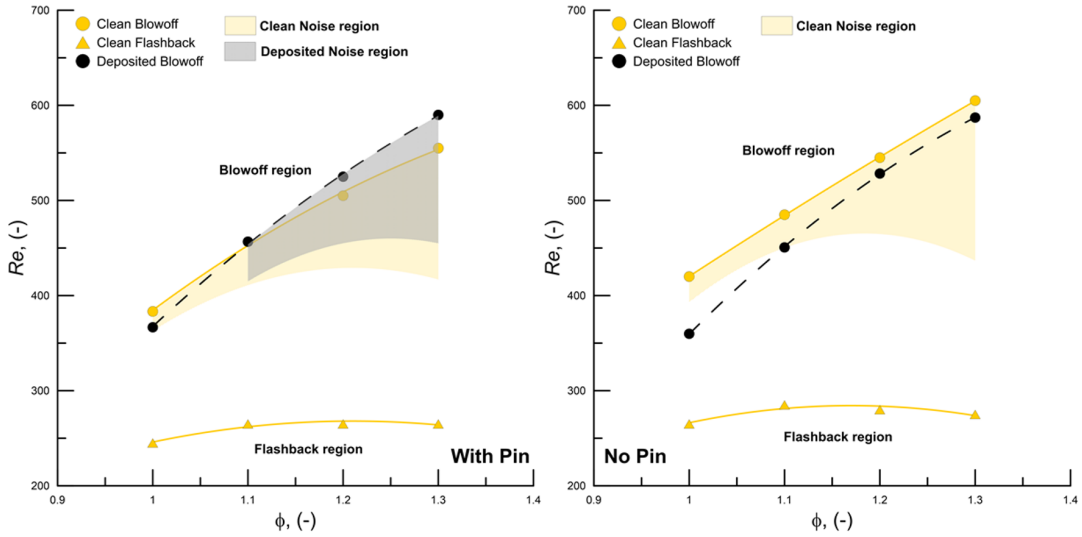

Figure 3.8: Overlap of plates' II and I stability maps in deposited and non-deposited conditions for $L = 35$ cm. The map on the left evaluates the use of the interior support pin inside plate's II chamfer during its electrodeposition procedure, while the map on the right investigates the absence of such pin during plate's I deposition. The non-deposited plate is associated to yellow symbols while the deposited plate is associated to black symbols. The yellow and grey shaded areas correspond to the non-deposited and deposited plates' self-sustained unstable combustion regions, respectively.

For the plate reconstructed with the use of the interior support pin, the burner does not present significant changes in its stability, exhibiting a blowoff limit and a noise region fairly similar to the ones in its non-deposited condition. However, for the plate reconstructed without the pin, there is a slight decrease in the flame's blowoff limit, particularly for leaner regimes, and a total suppression of the combustion instability region present in its clean condition.

This might indicate that the chamfer filling architecture affects the flame-plate heat balance and relevantly impacts the local thermoviscous effects, consequently changing the burner's acoustic resistance. However, using the Image J software to analyse pictures of the deposition performed without the pin, its bottom diameter was determined equal to 5.28 mm[2] and thus smaller than the one presented by the plate in non-deposited conditions ($d = 6$ mm).

Hence, it is considered more probable that the observed noise extinction was due to a disruption of the flame-burner acoustic coupling mechanism and not due to an increase in the system's acoustic damping. Is is assumed that the exhibited diameter change, albeit the deposition being porous, resulted in a relevant area reduction at the plate's bottom which translated into an increase of the incoming reactant flow's velocity field at the burner's outlet. This led to an increase in the flame's height which significantly changed its dynamics, reducing its blowoff limit and altering its FTF's phase (and possibly its gain), as previously described by Noiray *et al.* [8]. This phase change induced by the variation of the flame's convective time delay, altered the frequency distribution of the flame-generated PW and ended its former overlap with the (unaltered) burner's frequency bandwidth.

Pulsed current filling vs Constant current filling

The final case-study intended to assess the influence of the plate's chamfer filling morphology in the flame's stability. For that, plates' II and I chamfers were deposited with Samples C and D, respectively, both using the support pin inside its perforations during the deposition procedure. As described in Sections 2.2.1 and 3.1, Sample C was obtained in a pulsed mode and exhibits no interconnectivity between its pores, while Sample D was produced in a galvanostatic mode and does present interconnectivity between its pores. Moreover, from a qualitative analysis of Figure 3.3, it is safe to add that the former sample shows a lower mean pore dimension than the latter one; such that Sample C qualitatively presents a lower porosity than Sample D.

Following this, the chamfer-filled plates' FSDs were acquired for the defined resonant duct length and compared to their respective non-deposited behaviour. Results are presented in Figure 3.9.

For both chamfer-reconstructed plates, their associated blowoff limits remain reasonably identical to the ones exhibited in non-deposited conditions. However, while the plate whose foam presents lower porosity essentially preserves its thermoacoustic instability region size and location, the plate whose foam presents higher porosity exhibits a total suppression of this region.

This suggests that the chamfer filling morphology strongly conditions the local thermoviscous effects and consequently the burner's acoustic resistance. Contrarily to the initial illations obtained in the former case-studies, this conclusion is believed to be accurate since it somewhat confirms the findings presented by Kuczmarski and Johnston [30], that a structure's ability to dissipate acoustic energy increases with its pore interconnectivity and with an appropriate tuning of its pore size, and by Noiray *et al.* [8], that the burner's acoustic resistance is mainly conditioned by the thermoviscous effects in the anchoring plate's perforation inner wall boundary layer.

[2]The Re considered in this chamfer-reconstructed plate FSD was adjusted to take into account this diameter variation.

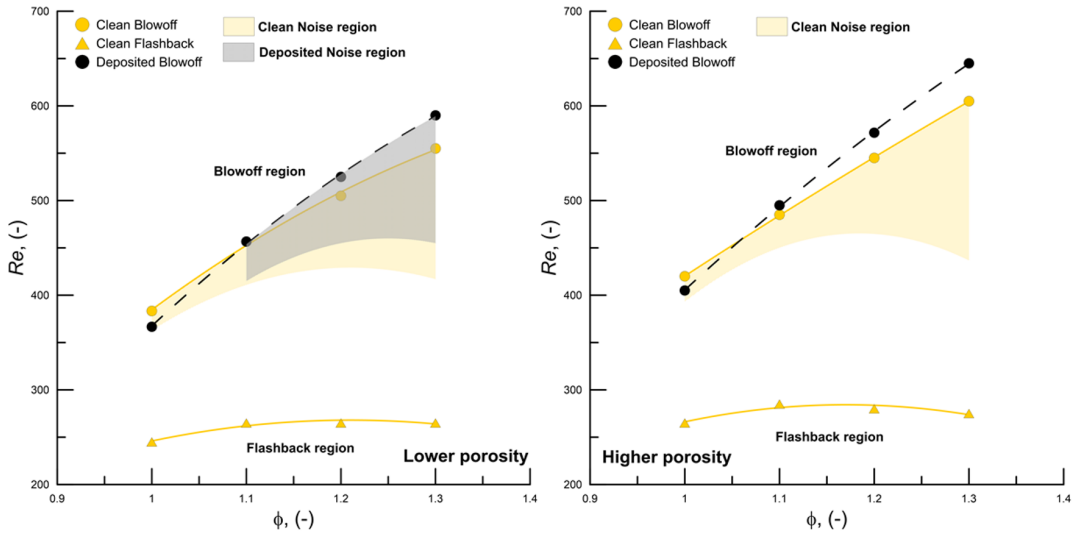

Figure 3.9: Overlap of plates' II and I stability maps in deposited and non-deposited conditions for $L = 35$ cm. The map on the left analyses the chamfer reconstruction of plate II with a low porosity foam, while the map on the right studies the chamfer reconstruction of plate I with a high porosity foam. The non-deposited plate is associated to yellow symbols while the deposited plate is associated to black symbols. The yellow and grey shaded areas correspond to the non-deposited and deposited plates' self-sustained unstable combustion regions, respectively.

3.2.3 Solution testing

In the third and final case-study, positive results were obtained for $L = 35$ cm, since plate's I chamfer-reconstruction with Sample D was able to completely suppress the self-sustained thermoacoustic instabilities, which naturally arise in its non-deposited condition, by apparently increasing the system's acoustic damping. Hence, a comparison between this new design's stability performance and the more commercially used straight edge perforation design was required.

To do so, the SE plate's FSD was compared with plate's I FSD when chamfer-filled with Sample D, for the defined resonant duct length $L = 35$ cm, in Figure 3.10.

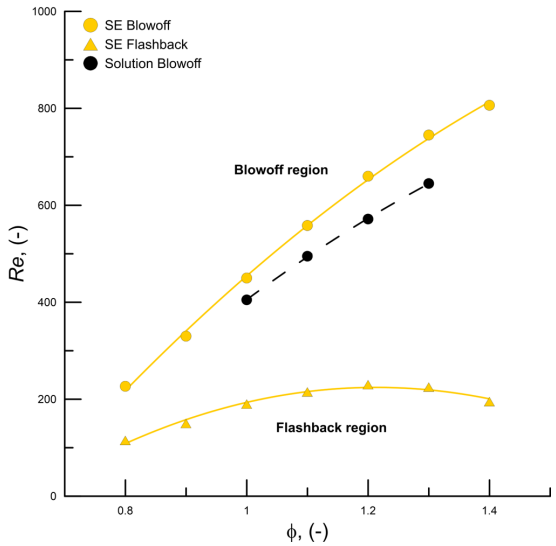

Figure 3.10: Overlap between the flame stability maps of the SE plate and the high porosity chamfer-reconstructed plate I for $L = 35$ cm. The SE plate is associated to yellow symbols while the deposited plate I is associated to black symbols.

For the tested equivalence ratios, although both plates present no unstable combustion regions, the SE plate still presents a higher flame stability than the chamfer-reconstructed plate I.

Nonetheless, it should be noted that, as exposed in Section 3.1, the chamfer-reconstruction performed by Sample's D deposition on plate I was not complete (reconstruction proximity $= 88.83\%$), being unable to fill its chamfer to a point where its top diameter coincided with its bottom diameter d. Considering this and the obtained results, it is considered possible that, in case of a complete reconstruction of such chamfer, plate's I blowoff limit would increase to a position substantially closer to the SE plate's blowoff limit.

Chapter 4

Conclusions

The ultimate goal of this work was to serve as a basis for the creation of an implementable, simple and flexible passive solution which minimizes the development of self-sustained thermoacoustic instabilities in modern open flame multiperforated plate burners. To achieve this, a study was performed in an unconfined single-point injection configuration regarding the influence of specific functional manipulations of the inner wall surface of the anchoring plate's perforation on flame stability. A depiction of the procedure followed in the intended stability analyses was presented, as well as a detailed description of the method used to perform the desired inner wall surface depositions. Before evaluating the flame's stability under different working conditions (Re, ϕ, resonant cavity size, flame anchoring plate, deposition sample), a characterization of the deposition samples was conducted. Results showed the existence of two different compositions: Sample A was essentially composed by Co arrays while Samples B, C and D were mainly composed by a Zn-derived (simonkolleite). Although all samples presented a 3D porous structure typical of foams constructed by the dynamic hydrogen bubble template method, Sample A presented a honeycomb-like structure with relative homogeneity, while Samples B, C and D presented a morphology composed by hexagon-like sub-units, typical of simonkolleite, with only Sample D presenting interconnectivity between its pores. In the stability analysis, an initial characterization of the anchoring plates used was followed by the presentation of three deposition case-studies, with variations regarding the thermal behaviour of the deposited material, the architecture of its macrostructure and the morphology of its microstructure. The latter analysis provided this work's most relevant conclusions, which are summarized and listed below:

- For the thickness range characteristic of industrial applications of electrodepositions, flame stability in an upward chamfered plate isn't relevantly affected by the chamfer's coating thermal conductivity (λ) or its variation during operation ($\frac{\partial \lambda}{\partial T}$).
- A porous reconstruction of an upward chamfered plate's chamfer, which leads to a decrease in the incoming fresh flow crossing area at the plate's bottom, might translate into a relevant increase of the flame's height and consequently change its dynamics. For a working condition specifically characterized by thermoacoustic instabilities, this change may alter the frequency distribution of the flame-generated PW to a point where its former coupling with the (unaltered) burner's acoustics

may cease to exist, stabilizing the combustion process.

- A porous reconstruction of an upward chamfered plate's chamfer, with a high pore interconnectivity level and an appropriately tuned pore size, mitigates the flame's ability to develop self-sustained thermoacoustic instabilities, apparently by increasing the local thermoviscous effects and consequently enhancing the burner's acoustic damping.

4.1 Future Work

The present work investigated an unexplored application of a widely implemented surface engineering technique. The obtained results invite a further study of the addressed topics.

At an experimental level, the positive results obtained for the porous chamfer-reconstruction with a high interconnectivity level and an appropriate pore size should be further explored. The deposited plate's stability should be evaluated for a wider range of cavity sizes, to confirm that its mitigation of the formerly present self-sustained thermoacoustic instabilities is in fact due to an increase of the burner's acoustic damping. Also, a sensitivity analysis of the electrodeposition's current density and exposure time is suggested, to evaluate these parameters influence on the structure's morphology but particularly on its ability to dissipate acoustic energy.

At a numerical level, an appropriate model of the chamfer-reconstructed plate whose foam presents a high interconnectivity level and an appropriate pore size should be performed. It is suggested to use the instability model developed by Noiray *et al.* [19] to compute the minimum increase required in this plate's acoustic damping to completely suppress its ability to develop self-sustained thermoacoustic instabilities, in non-deposited conditions. Then, assuming a linear behaviour, this acoustic damping should be extrapolated for a multiperforated plate case and, using the model developed by Ferreira [20], an evaluation of the system's stability for several cavity sizes is recommended to confirm that a multiperforated plate with the presented deposition would also be able to completely suppress its unstable behaviour.

Bibliography

[1] *World Population Prospects: The 2017 Revision*. United Nations, Department of Economic and Social Affairs, 2017.

[2] A. Liñán and F. A. Williams. Fundamental aspects of combustion. *New York, NY (United States); Oxford University Press*, 1993.

[3] S. T. Omaye. Metabolic modulation of carbon monoxide toxicity. *Toxicology*, 180(2):139–150, 2002.

[4] J. M. Pires and E. C. Fernandes. Combined effect of equivalence ratio and velocity gradients on flame stability and emission formation. *Fuel*, 222:800–809, 2018.

[5] K. R. A. M. Schreel, E. L. van den Tillaart, and L. P. H. De Goey. The influence of burner material properties on the acoustical transfer function of radiant surface burners. *Proceedings of the Combustion Institute*, 30(2):1741–1748, 2005.

[6] T. Schuller, D. Durox, and S. Candel. Self-induced combustion oscillations of laminar premixed flames stabilized on annular burners. *Combustion and Flame*, 135(4):525–537, 2003.

[7] D. Durox, T. Schuller, and S. Candel. Self-induced instability of a premixed jet flame impinging on a plate. *Proceedings of the Combustion Institute*, 29(1):69–75, 2002.

[8] N. Noiray, D. Durox, T. Schuller, and S. Candel. Passive control of combustion instabilities involving premixed flames anchored on perforated plates. *Proceedings of the Combustion Institute*, 31(1): 1283–1290, 2007.

[9] A. A. Putnam. *Combustion-driven oscillations in industry*. Elsevier Publishing Company, 1971.

[10] S. M. Candel. Combustion instabilities coupled by pressure waves and their active control. In *Symposium (International) on Combustion*, volume 24, pages 1277–1296. Elsevier, 1992.

[11] T. Schuller, D. Durox, and S. Candel. Dynamics of and noise radiated by a perturbed impinging premixed jet flame. *Combustion and Flame*, 128(1-2):88–110, 2002.

[12] E. C. Fernandes and R. E. Leandro. Modeling and experimental validation of unsteady impinging flames. *Combustion and Flame*, 146(4):674–686, 2006.

[13] K. R. McManus, T. Poinsot, and S. M. Candel. A review of active control of combustion instabilities. *Progress in Energy and Combustion Science*, 19(1):1–29, 1993.

[14] G. A. Richards, D. L. Straub, and E. H. Robey. Passive control of combustion dynamics in stationary gas turbines. *Journal of Propulsion and Power*, 19(5):795–810, 2003.

[15] V. Meille. Review on methods to deposit catalysts on structured surfaces. *Applied Catalysis A: General*, 315:1–17, 2006.

[16] M. F. Montemor, S. Eugénio, N. Tuyen, R. P. Silva, T. M. Silva, and M. J. Carmezim. Nanostructured transition metal oxides produced by electrodeposition for application as redox electrodes for supercapacitors. *Handbook of Nanoelectrochemistry: Electrochemical Synthesis Methods, Properties, and Characterization Techniques*, pages 681–714, 2016.

[17] B. J. Plowman, L. A. Jones, and S. K. Bhargava. Building with bubbles: the formation of high surface area honeycomb-like films via hydrogen bubble templated electrodeposition. *Chemical Communications*, 51(21):4331–4346, 2015.

[18] J. W. S. Baron Rayleigh. *The theory of sound*, volume 2. Macmillan, 1896.

[19] N. Noiray, D. Durox, T. Schuller, and S. Candel. Self-induced instabilities of premixed flames in a multiple injection configuration. *Combustion and Flame*, 145(3):435–446, 2006.

[20] M. G. C. Ferreira. Thermoacoustic self-sustained instabilities of conical flames in multi-perforated plate buners. Master's thesis, Instituto Superior Técnico, Universidade de Lisboa, July 2017.

[21] H. Tijdeman. On the propagation of sound waves in cylindrical tubes. *Journal of Sound and Vibration*, 39(1):1–33, 1975.

[22] D. Maa. Potential of microperforated panel absorber. *The Journal of the Acoustical Society of America*, 104(5):2861–2866, 1998.

[23] F. M. White. Fluid mechanics. 5th. *Boston: McGraw-Hill Book Company*, 2003.

[24] E. W. Lemmon, R. T. Jacobsen, S. G. Penoncello, and D. G. Friend. Thermodynamic properties of air and mixtures of nitrogen, argon, and oxygen from 60 to 2000 k at pressures to 2000 mpa. *Journal of Physical and Chemical Reference Data*, 29(3):331–385, 2000.

[25] J. W. Niemantsverdriet. Spectroscopy in catalysis: An introduction. 3rd, completely revised and enlarged edition edn. *Wiley-VCH, Weinheim Weckhuysen BM (2009) Chemical imaging of spatial heterogeneities in catalytic solids at different length and time scales. Angewandte Chemie International Edition*, 48(27):4910–4943, 2007.

[26] W. Qin, C. Yang, X. Ma, and S. Lai. Selective synthesis and characterization of metallic cobalt, cobalt/platinum, and platinum microspheres. *Journal of Alloys and Compounds*, 509(2):338–342, 2011.

[27] L. M. Marques, M. M. Alves, S. Eugénio, S. B. Salazar, N. Pedro, L. Grenho, N. P. Mira, M. H. Fernandes, and M. F. Montemor. Potential anti-cancer and anti-candida activity of zn-derived foams. *Journal of Materials Chemistry B*, 6(18):2821–2830, 2018.

[28] P. A. L. F. L. Santos. Stability analysis of premixed laminar propane flames. Master's thesis, Instituto Superior Técnico, Universidade de Lisboa, October 2017.

[29] C. Y. Ho, R. W. Powell, and P. E. Liley. Thermal conductivity of the elements. *Journal of Physical and Chemical Reference Data*, 1(2):279–421, 1972.

[30] M. A. Kuczmarski and J. C. Johnston. Acoustic absorption in porous materials. *National Aeronautics and Space Administration*, 2011.